

# Attention-Based Reconstruction of Full-Field Tsunami Waves from Sparse Tsunameter Networks

Edward McDugald<sup>1,2</sup>, Arvind Mohan<sup>2</sup>, Darren Engwirda<sup>3,5</sup>, Agnese Marcato<sup>4</sup>,  
Javier Santos<sup>4</sup>

<sup>1</sup>University of Arizona

<sup>2</sup>Computer, Computational, and Statistical Sciences Division, Los Alamos National Laboratory

<sup>3</sup>Theoretical Division, Los Alamos National Laboratory

<sup>4</sup>Earth and Environmental Sciences, Los Alamos National Laboratory

<sup>5</sup>Environment, Commonwealth Scientific & Industrial Research Organisation

## Key Points:

- An attention-based neural network specialized for sparse sensing is implemented to reconstruct tsunami waves from sparse observations.
- We test our model on tsunami simulations whose epicenters differ from those used in training, replicating realistic forecasting conditions.
- We compare our method to the Linear Interpolation with Huygens-Fresnel Principle to generate virtual waveforms, showing improved accuracy.

**Abstract**

We investigate the potential of an attention-based neural network architecture known as the Senseiver to perform sparse sensing tasks in the context of tsunami forecasting. In particular, we focus on the Tsunami Data Assimilation Method, where forecasts are derived from tsunami meter networks. We used our model to generate high-resolution tsunami waves from incredibly sparse observations, whose epicenters are not included in the training set. We also show significantly improved accuracy in the generation of dense observation networks by comparison to the Linear Interpolation with Huygens-Fresnel Principle.

**Plain Language Summary**

While machine learning methods have been used to provide accurate forecasts of tsunami waveforms at fixed observation points, full-field reconstruction of tsunami waves from sparse observations have yet to be demonstrated by machine learning methods. This task is relevant to the tsunami data assimilation method, where in-ocean tsunami meter observations are combined with numerical methods to forecast tsunamis. In this work, we use an attention-based neural network architecture known as the Senseiver to generate remarkable tsunami wave reconstructions given extremely sparse tsunami meter measurements corresponding to real sensor locations. To demonstrate the utility of our method for forecasters using the tsunami data assimilation method, we conduct experiments where the Senseiver is used to generate virtual waveforms in a sparse observation network, and compare the results to an established interpolation method used for the same task.

**1 Introduction**

Tsunami early warning systems are important tools for minimizing the human and economic costs of tsunamis. The majority of existing systems employ partial differential equation (PDE) based solvers, in which an initial ocean surface displacement is derived based on estimates of the underlying earthquake dynamics, and a shallow water equation (SWE) type PDE model is integrated to predict the propagation of wave fronts over the ocean basin. Various PDE-based models are currently employed both operationally and throughout the research communities, including NOAA's MOST system (Titov & Gonzalez, 1997), the GeoCLAW solver (Berger et al., 2011; LeVeque et al., 2011), and the Gerris/Basilisk frameworks (Popinet, 2012, 2020). These methods suffer from uncertainties in the estimation of seismic parameters, as well as steep computational costs in integrating the PDEs. The tsunami data assimilation method (TDAM) (Maeda et al., 2015) was introduced to mitigate these issues. In TDAM, tsunami meter observations are combined with 2d Linear Long Wave equations (LLW) to forecast arrival times and wave amplitudes at selected observation gauges, bypassing the needs for source inversion and expensive integration of PDEs.

Although TDAM is effective in regions of the ocean with dense observation networks, its accuracy is limited in sparse observation networks. In such regions, there is a need for sparse sensing capabilities to make TDAM a practical tool for forecasters. Although machine learning (ML) methods have been proposed to provide tsunami waveform forecasts at fixed observation gauges (Liu et al., 2021), (Rim et al., 2022), to the best of our knowledge no ML-based solutions have been proposed for sparse sensing problems in the context of tsunami waves. In this paper, we explore the use of the Senseiver, an attention-based neural network designed for sparse sensing tasks, to reconstruct high resolution tsunami waves from sparse tsunami meter observations. We also test the use of the Senseiver in generating dense observation networks and compare its performance against the Linear Interpolation with Huygens-Fresnel Principle (LIHFP), proposed in (Wang et al., 2019).

Our experiments are set up to mimic a forecasting workflow where a pretrained model is used to reconstruct full-field tsunami waves from measurements of the Deep-ocean Assessment and Reporting of Tsunami Network (DART) buoys. Our model is tested on measurements whose tsunami epicenters differ from those used in the training set, showcasing the Senseiver's capability to extrapolate to initial conditions not seen in training. In addition to evaluating the  $L^1$  error and physical consistency of high-resolution reconstructions, we demonstrate an improvement in the generation of virtual waveforms at artificial observation points compared to the LIHFP method. In particular, the virtual waveforms recovered by our method exhibit approximately a two-fold decrease in average wave height, arrival time, and maximum amplitude errors.

In the conclusion, we recommend future experiments to probe the utility of the Senseiver in related forecasting problems, such as direct forecasting of high-resolution tsunami waves from tsunamieters, early warning systems from GNSS data, and optimal sensor placements.

## 2 Generating Full-Field Training Data

Observational datasets associated with historical tsunami events are typically very sparse, being collected only at discrete buoy stations (e.g. the DART network (NOAA, 2011)) distributed throughout the global ocean. Due to its sparsity, such data is insufficient for model training, for which a dense spatio-temporal description of sea surface height evolution is required.

In this work, we use a calibrated PDE-based model to generate the full-field training data needed, solving the depth-integrated equations that describe barotropic ocean dynamics

$$\frac{\partial u}{\partial t} + (u \cdot \nabla) u + f u^\perp = -(1 - \beta) g \nabla(h + z_b) + c_d \frac{|u|}{h} u + \nu_k^u \nabla^k u, \quad (1)$$

$$\frac{\partial h}{\partial t} + \nabla \cdot (u h) = 0. \quad (2)$$

This system includes the gravity wave processes associated with sea surface waves, as well as nonlinear contributions accounting for momentum advection, the Coriolis tendency, bottom drag, dissipation and self-attraction and loading. The reader is referred to Text S1 in the supporting information for additional detail. The PDE-based model was calibrated using DART sensor output associated with historical events, leading to high fidelity reconstructions. Detailed verification is provided in Text S2 and Figures S1-S2 in the supporting information.

Our data consists of 16 time integrations of equations (1) and (2), where the initial conditions are 5m Gaussian ocean height displacements defined by epicenter location. Eight epicenters were selected by randomly querying a lookup table of USGS earthquake records, and the test data is obtained by randomly perturbing those epicenters. The training epicenters are listed in Table S1 of the supporting information, and the test epicenters are listed in Table 1. For the mesh used in the SWE solver, each frame is output as an unstructured list of 163,842 tuples, consisting of a longitude/latitude coordinate and a wave height. We subsample each frame by a factor of 2, yielding frames consisting of 81,921 pixels. For each training epicenter, the simulation is run for 289 time steps, with a time step of 50s, effectively giving 4 hour simulations.

### 3 Methods

#### 3.1 The Senseiver

The sparse sensing problem for tsunami waves can be stated as follows: given a discrete set of observations of the ocean state  $s = \{s_1, s_2, \dots, s_N\}$  at locations  $\mathbf{x}^s = \{\mathbf{x}_1^s, \mathbf{x}_2^s, \dots, \mathbf{x}_N^s\}$  and time  $t$ , reconstruct a set of state outputs  $\hat{s} = \{\hat{s}_1, \hat{s}_2, \dots, \hat{s}_M\}$  at a set of query points  $\mathbf{x}^q = \{\mathbf{x}_1^q, \mathbf{x}_2^q, \dots, \mathbf{x}_M^q\}$  such that  $M \gg N$ . In this work, the input state  $s(\mathbf{x}^s, t)$  is taken to be the ocean surface height measured at DART buoy locations, and the query state  $\hat{s}(\mathbf{x}^q, t)$  is the ocean surface height throughout the remainder of the global ocean domain. Noting that DART buoys number only a few dozen, and that even relatively coarse coverage of the global ocean requires at least several hundred thousand discrete points, the reconstruction problem is seen to be extremely sparse.

The Senseiver (Santos et al., 2023), an attention-based neural network, has been developed to solve such problems — employing a multi-level encoder-decoder architecture to reconstruct dense output from sparse observations. The core concept of the Senseiver is to combine the attention operation (Vaswani et al., 2017) with data compression. Some key attributes of the attention operation that make it powerful for sparse sensing tasks are: (1) it treats positional information as a feature, (2) it is grid agnostic, making it amenable to data on arbitrary mesh structures, and (3) it can make long-range spatial associations immediately (unlike CNNs where spatially distinct elements are not combined until very deep in the network). The cost of these capabilities is that the attention operation scales quadratically with the size of its input. The Senseiver mitigates this computational bottleneck by encoding the input into latent arrays of reduced size, wherein the bulk of attention operations occur. In brief, the model operates as follows:

1. A positional encoder  $P_E$  is used to map the location of observations to a spatial encoding vector  $\mathbf{a}^s$ , with  $s \in \mathbb{R}^N$ .
2. An attention-based encoder  $E$  is used to map the encoded observation/location pairs  $(s_i, \mathbf{a}_i^s)$  to a latent matrix  $\mathbf{Z}$ .
3. The positional encoder  $P_E$  is used to map query locations to a spatial encoding vector  $\mathbf{a}^q$ , with  $q \in \mathbb{R}^M, M \gg N$ .
4. An attention-based decoder  $D$  is used to reconstruct outputs at the encoded query locations  $\mathbf{a}^q$ .

The positional encoder  $P_E$  implements a trigonometric encoding of the spatial coordinates, and the encoder and decoder operators  $E, D$  contain trainable layers in the form of multi-layer perceptrons within their attention blocks. The reader is referred to (Santos et al., 2023) for in-depth discussions of the Senseiver architecture, summarised here as follows

$$\mathbf{a}^s = P_E(\mathbf{x}^s), \quad (3)$$

$$\mathbf{Z} = E(s, \mathbf{a}^s), \quad (4)$$

$$\mathbf{a}^q = P_E(\mathbf{x}^q), \quad (5)$$

$$\hat{s}(\mathbf{x}^q, t) = D(\mathbf{Z}, \mathbf{a}^q). \quad (6)$$

While previous experiments of the Senseiver used data residing on a structured grid, the flexibility of the architecture allows one to seamlessly build a model on unstructured data. Further, the choice of coordinates for the positional encoder are not restricted to the underlying spatial coordinates. For this problem, we added encodings for the ocean bathymetry in addition to latitude and longitude. We also mask out land pixels, training only on data corresponding to ocean pixels. A schematic for the Senseiver workflow is provided in Figure 1.

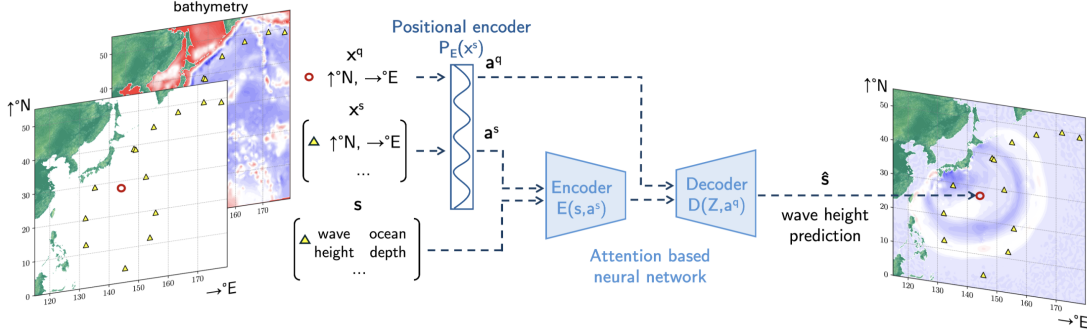


**Figure 1.** High-level overview of the Senseiver architecture for tsunami reconstruction. The sensor values along with their encoded positions are processed by the encoder into a latent array  $Z_1$  of fixed size. The encoded query locations are processed by the decoder, where they are first mapped to another latent array  $Z_2$ , and attention operations are applied to  $Z_1$  and  $Z_2$  to output an estimate of wave height at the query location(s).

### 3.2 Model Training

While the Senseiver is capable of reconstructing dense output from sparse observations, it must first learn the behavior of the system through a training procedure in which the weights of the model are optimized by minimizing an error measure, here taken to be the mean-squared error

$$\mathcal{L} = \sum \left( s(\mathbf{x}^q, t) - \hat{s}(\mathbf{x}^q, t) \right)^2, \quad (7)$$

$$\text{where } \hat{s}(\mathbf{x}^q, t) = D(E(s(\mathbf{x}^q, t), P_E(\mathbf{x}^s)), P_E(\mathbf{x}^q)). \quad (8)$$

Noting that the loss (7) is a summation over the query points  $\mathbf{x}^q$ , here taken to be a dense set covering the global ocean domain, training the model requires that a dense set of state estimates  $s(\mathbf{x}^q, t)$  be available, provided in this work by a PDE simulation. We minimize the loss using the stochastic gradient descent algorithm Adam (Kingma & Ba, 2014), with an 80/20 train/test split. The number and ordering of query points and data frames used in training are selectable as hyper-parameters, the details of which are summarized in Text S3 of the supporting information.

### 3.3 Experiments

Clearly, any pre-trained model used in a real life forecasting scenario must be able to operate on data whose initial conditions are not observed in training. To test the Senseiver on novel initial conditions, we perturbed the eight training epicenters by randomly sampling an angle and radial distance to obtain new epicenters that are distinct from the training epicenters. These epicenters are depicted visually in relation to the training epicenters in Figure 2. The distances of the unseen epicenters from their closest training epicenter range from 2.78 miles to 119.97 miles, and are listed for all test epicenters in Table 1

The error metric that we use to evaluate a given reconstruction is the mean absolute error, scaled by the absolute maximum wave height. The absolute errors are averaged only over pixels achieving a value of at least  $1 \times 10^{-4}$  in the true field. Since most of the waveheight over the global ocean is identically 0, this pixel restriction mitigates the issue of artificially low error. For each reconstruction, we compute the absolute dif-

ference between the true and reconstructed wave height fields, and divide by the maximum absolute true wave height for that frame. As a formula, this is:

$$\text{Error}(x, y, t) = \frac{|h(x, y, t) - \hat{h}(x, y, t)|}{\max(|h(x, y, t)|)}. \quad (9)$$

While the full-field reconstructions obtained by the Senseiver are notable in their own right, existing tsunami-based forecasting methods primarily aim to estimate the arrival time and maximum amplitude of tsunami waveforms at fixed observation points. The tsunami data assimilation method (Maeda et al., 2015) has been used to generate such waveforms given dense observation networks. For regions with sparse sensor coverage, the Linear Interpolation with Huygens Fresnel Principal (LIHFP) was proposed to augment the sparse observation network, and thus improve the accuracy of the tsunami data assimilation method. In brief, for a pair of real observation locations, LIHFP estimates the arrival time for a virtual waveform between the real locations by using a distance-weighted combination of the real arrival times. The full virtual waveform is then obtained by interpolating the real waveforms, taking into account their relative distances, arrival times, and bathymetry values. For a more detailed description of the method, the reader is referred to (Wang et al., 2019). To strengthen the case for the Senseiver in contemporary forecasting methods, we supplement our reconstruction experiments with the generation of six virtual waveforms and compare our waveforms to those obtained via LIHFP.

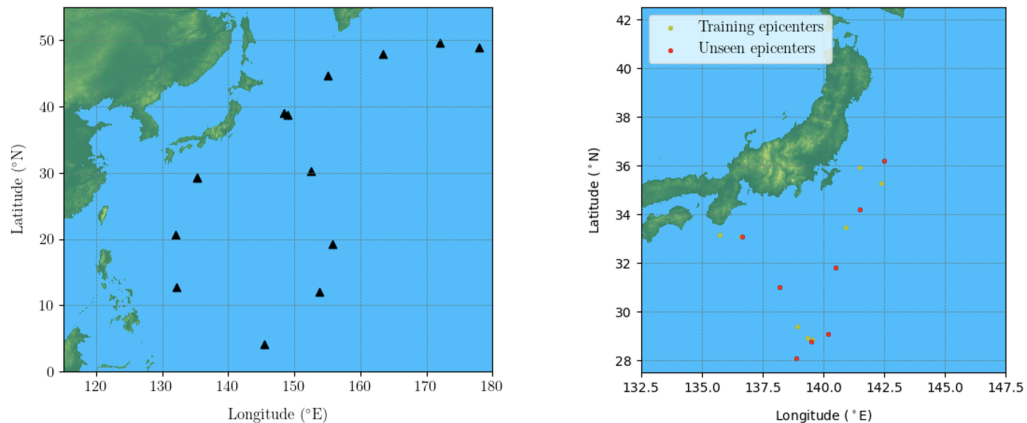


**Figure 2.** The left panel depicts coverage of DART Buoys, denoted by black triangles. The right panel depicts the training (black) and unseen (red) epicenters used for synthetic tsunami generation.

## 4 Results

Averaging the reconstruction loss (9) across all 289 frames of all 8 of the unseen epicenters yields a global experiment error of  $6.02 \times 10^{-2}$ . A significant contributor to the error comes from early time frame reconstructions, where the sensors receive null to negligible signal from the tsunami wave. This is an unavoidable issue with any assimilation method depending only on tsunami sources. The mean time for the error to remain below  $1 \times 10^{-1}$  is 83.3 minutes, with significant outlier times of 202.5 and 200.8 minutes. Excluding these outliers, the mean time drops to 43.88 minutes. The key results of the reconstruction experiments for all 8 simulations can be found in the first 7 columns of Table 1.

In Figure 3, we show sample reconstructions for the test simulation with epicenter ( $141.5^{\circ}\text{E}, 34.2^{\circ}\text{N}$ ) at 75 minutes, 150 minutes, and 225 minutes, a sample waveform reconstruction at DART buoy ( $135.2^{\circ}\text{E}, 29.3^{\circ}\text{N}$ ), the reconstruction error over time, and the physical consistency error over time. We selected this epicenter for presentation in the main text since it is separated from its closest neighbor in the training set by 61.02 miles, which is closest to the median distance over all test epicenters. Equivalent figures for the other test epicenters are provided in Figure S3-S9 of the supporting information. Inspection of the reconstructions shows that both the phase field support, number of periods, and amplitude are well approximated by the Senseiver. As seen in the error plot, the reconstruction error drops rapidly during the first  $\approx 50$  minutes of the simulation, reflecting the ill-posedness of early time reconstruction. For this epicenter, the error stays below the  $1 \times 10^{-1}$  threshold at  $t = 40.8$  minutes. While the focus of this letter is not on resolution of early time-frame reconstruction problems, we do suggest ways in which the Senseiver architecture can be used to solve such problems in the conclusion. We also track the physical consistency of the model by plotting the error of the continuity equation (2). We find that the Senseiver reconstructions generally produce lower physical consistency errors than the PDE model itself.

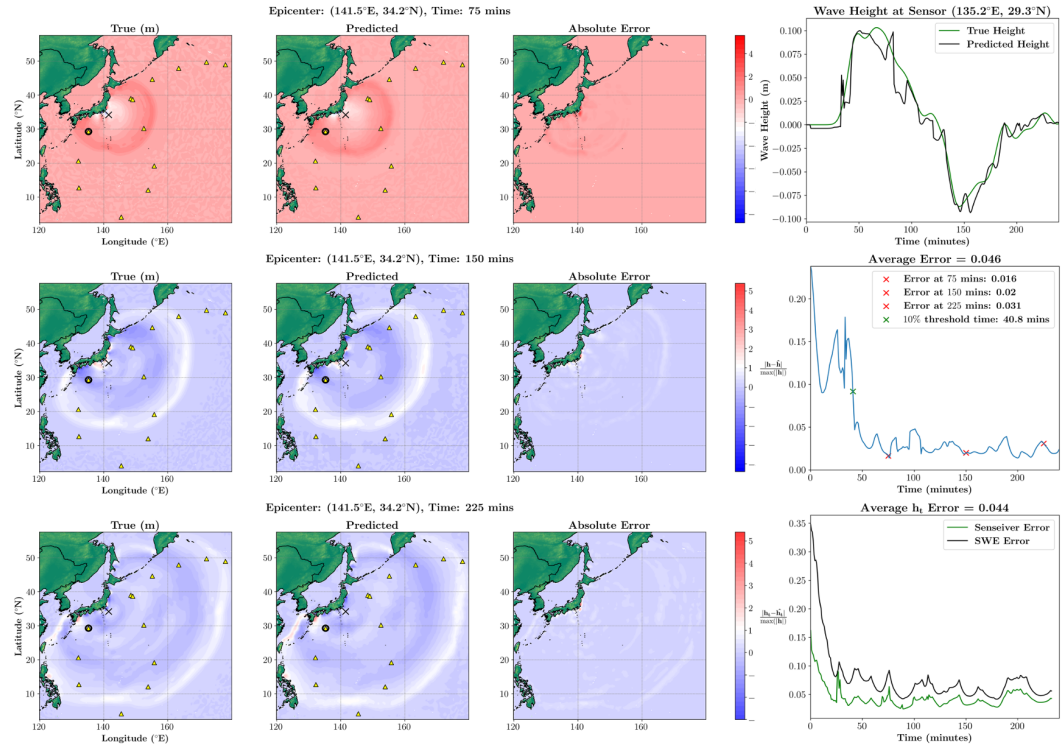


**Figure 3.** Reconstructions at 75 minutes (top rows), 150 minutes (middle row), and 225 minutes for epicenter location ( $141.5^{\circ}\text{E}, 34.2^{\circ}\text{N}$ ). The left panel shows the true field, the middle panel shows the predicted field, and the right panel shows the absolute error. The epicenter location is indicated by an X, and yellow triangles note the sensors. The topmost panel on the right shows the waveform at fixed DART buoy with longitude-latitude coordinate ( $135.2^{\circ}\text{E}, 29.3^{\circ}\text{N}$ ). This buoy is distinguished in the reconstructions with a circle. The middle left panel shows the reconstruction error profile as a function of time with red x's indicating the times for the displayed reconstruction, and the green x notating the time where the error stay permanently below  $1 \times 10^{-1}$ . The bottom right panel shows the physical consistency error as a function of time.

To test the Senseiver against existing sparse sensing methods in the literature, we compared its performance against the LIHFP method (Wang et al., 2019) of obtaining dense observation networks from sparse observation networks. Among the DART buoys registering full waveforms in our simulations, we selected 6 midpoints to use as locations for virtual observations, and compared the Senseiver output at those locations to the corresponding LIHFP estimates. Across all simulations and time steps, LIHFP yielded a mean absolute error of  $2.16 \times 10^{-1}$  meters, whereas the Senseiver yielded a mean absolute error of  $1.21 \times 10^{-1}$  meters. We also found a significant improvement in estimating arrival times and maximum amplitudes across all simulations and virtual observations. The mean absolute error for arrival time was 9.983 minutes for the Senseiver, and 16.384 minutes for LIHFP. The mean absolute error for maximum amplitude was  $1.37 \times 10^{-1}$  meters for the Senseiver and  $2.88 \times 10^{-1}$  meters for LIHFP. The key results of the virtual waveform experiments for all 8 simulations can be found in the last 6 columns of Table 1.

In Figure 4, we summarize the virtual waveform experiment for epicenter location ( $141.5^\circ E, 34.2^\circ N$ ). Across the 6 virtual waveforms generated for this epicenter, LIHFP yielded a mean absolute error of  $2.46 \times 10^{-1}$  meters, whereas the Senseiver yielded a mean absolute error of  $0.75 \times 10^{-1}$  meters. The mean absolute error for arrival time was 7.778 minutes for the Senseiver, and 16.528 minutes for LIHFP. The mean absolute error for maximum amplitude was  $0.91 \times 10^{-1}$  meters for the Senseiver and  $3.43 \times 10^{-1}$  meters for LIHFP. We also display the mean absolute errors in arrival time and maximum amplitude for each simulation and for each virtual waveform. Equivalent figures for the other test epicenters are provided in Figures S10-S16 of the supporting information.

Epicenter Number	Longitude	Latitude	Distance to Closest Training Epicenter	Mean Recon Error	Mean Physics Error	Trigger Time (mins)	Senseiver Arrival Time MAE (mins)	LIHFP Arrival Time MAE (mins)	Senseiver Max Amplitude MAE (m)	LIHFP Max Amplitude MAE (m)	Senseiver Wave Height MAE (m)	LIHFP Wave Height MAE (m)
			(miles)									
1	136.65	33.1	2.78	0.038	0.036	15.8	11.667	17.36	0.08	0.167	0.048	0.176
2	138.2	31	119.97	0.063	0.046	74.2	7.639	17.153	0.104	0.187	0.192	0.184
3	138.9	28.1	63.11	0.074	0.057	202.5	8.889	17.014	0.267	0.321	0.149	0.216
4	139.5	28.8	5.144	0.047	0.055	40.8	5.833	16.667	0.155	0.318	0.059	0.214
5	140.2	29.1	42.42	0.078	0.061	69.2	11.111	16.389	0.214	0.32	0.154	0.223
6	140.5	31.8	117.04	0.092	0.058	200.8	11.111	16.389	0.079	0.327	0.19	0.235
7	141.5	34.2	61.02	0.046	0.044	40.8	7.778	16.528	0.091	0.343	0.075	0.246
8	142.5	36.2	64.77	0.045	0.038	22.5	15.833	15.972	0.105	0.317	0.097	0.237

**Table 1.** Overview of Senseiver evaluation metrics. Columns 4-7 correspond to reconstruction experiments, and columns 8-13 correspond to LIHFP comparisons. MAE refers to mean absolute error, and Trigger Time refers to the time at which no reconstruction exceeds  $1 \times 10^{-1}$ .

## 5 Conclusion

We have exhibited an attention-based architecture that reconstructs high-resolution tsunami waves given sparse observation networks. We evaluated our model using standard  $L^1$ -based error metrics and by comparison to the LIHFP method. While ML methods have been proposed to forecast waveforms at fixed observation points (Liu et al., 2021; Rim et al., 2022), to the best of our knowledge this is the first ML-based solution to solve the sparse sensing problem at high resolution for tsunami forecasting. Moreover, we exhibited significant improvements in Senseiver-based virtual waveforms compared to LIHFP.

The simplest extension of this work would be to conduct experiments where the initial  $t = 0$  ocean displacements are varied in magnitude (as opposed to just varying

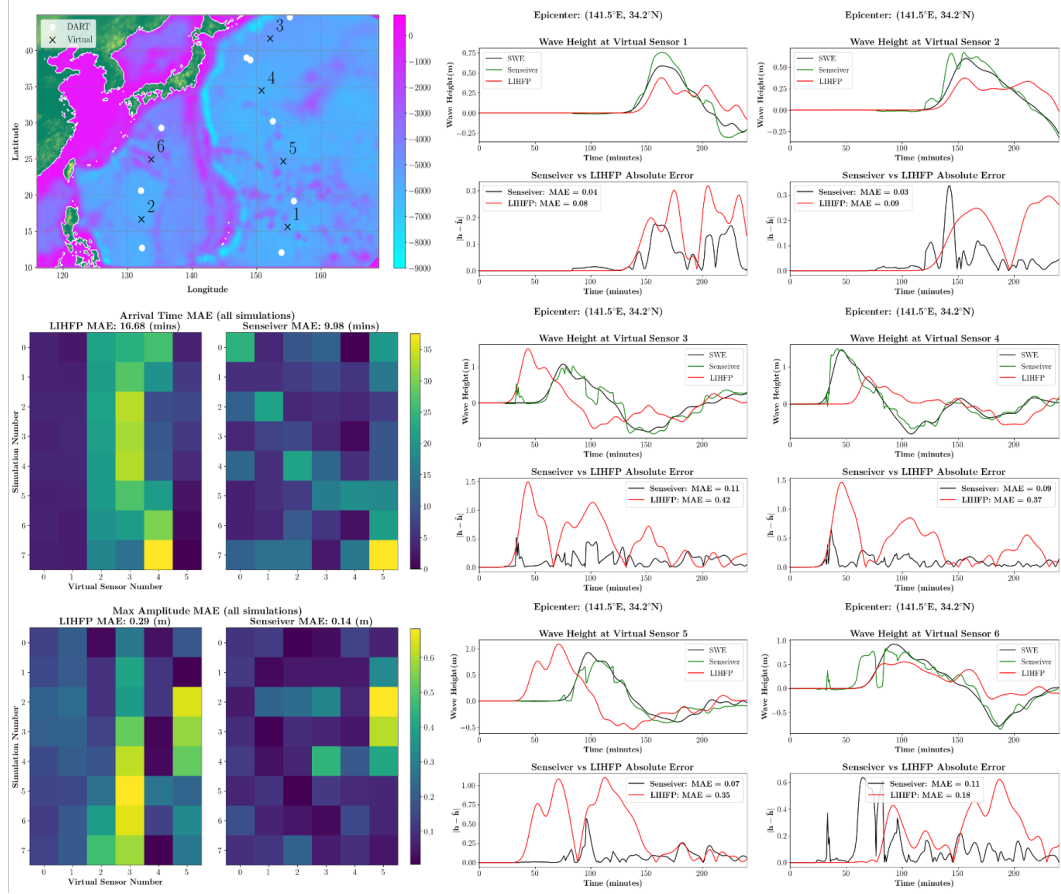


**Figure 4.** Comparison of LIHFP and Senseiver based virtual observation measurements. The top left panel displays the observation network over a bathymetry map. The middle and bottom panels of the left column show the mean absolute error in arrival time and maximum amplitude for all simulations and for all virtual observation points. The middle and right columns display Senseiver and LIHFP-based waveform reconstructions as well as their absolute errors for epicenter ( $141.5^{\circ}E, 34.2^{\circ}N$ ).

in location). In addition, including more epicenters in the training set and fewer time steps per simulation would be fruitful. To resolve the issue of early time-frame reconstructions, experiments should be conducted where the Senseiver is applied to non-tsunameter data. In (Rim et al., 2022) convolutional neural networks were applied to Global Navigation Satellite System (GNSS) data, allowing for accurate future waveform estimates given as little as 6 minutes of tsunami data. Similar experiments can be conducted with the Senseiver, where the GNSS data is used as input to reconstruct wave height fields during times where the wave front has not reached any tsunamieters. HF Radar (Wang, Imai, Miyashita, et al., 2023) and distributed acoustic sensing (Xiao et al., 2024) data sets could also be used for similar experiments. The Senseiver can also be used to deduce optimal buoy placements by allowing some or all of the sensor positions to be learned during training (Marcato et al., 2023). This would be a useful capability for regions with limited budgets for sensor deployments.

## Open Research Section

The code and data for this project will be made publicly available via github and zenodo after publication. In the meantime, reviewers can access the code at the following github repo <https://github.com/OrchardLANL/Senseiver>. Likewise, the data can be found at zenodo <https://zenodo.org/records/14189533>.

### Acknowledgments

This project was partially funded by the Artimis LDRD program at the Los Alamos National Laboratory. The Los Alamos Unlimited Release number for this work is LA-UR-24-32151. Andrew Arnold (University of Arizona PhD Student in Applied Mathematics) assisted in analyzing the virtual waveform experiments.

## References

Archambault, T., Filoche, A., Charantonis, A., Béréziat, D., & Thiria, S. (2024). Learning sea surface height interpolation from multi-variate simulated satellite observations. *Journal of Advances in Modeling Earth Systems*, 16(6), e2023MS004047. Retrieved from <https://agupubs.onlinelibrary.wiley.com/doi/abs/10.1029/2023MS004047> (e2023MS004047 2023MS004047) doi: <https://doi.org/10.1029/2023MS004047>

Barton, K. N., Pal, N., Brus, S. R., Petersen, M. R., Arbic, B. K., Engwirda, D., ... Schindelegger, M. (2022). Global barotropic tide modeling using inline self-attraction and loading in MPAS-Ocean. *Journal of Advances in Modeling Earth Systems*, 14(11), e2022MS003207.

Berger, M. J., George, D. L., LeVeque, R. J., & Mandli, K. T. (2011). The GeoClaw software for depth-averaged flows with adaptive refinement. *Advances in Water Resources*, 34(9), 1195–1206.

Bernard, E., & Titov, V. (2015, 10). Evolution of tsunami warning systems and products. *Philosophical transactions. Series A, Mathematical, physical, and engineering sciences*, 373. doi: 10.1098/rsta.2014.0371

Engwirda, D. (2017). JIGSAW-GEO: locally orthogonal staggered unstructured grid generation for general circulation modelling on the sphere. *Geoscientific Model Development*, 10(6), 2117–2140.

Fujii, Y., Satake, K., Sakai, S., Shinozawa, M., & Kanazawa, T. (2011). Tsunami source of the 2011 off the Pacific coast of Tohoku Earthquake. *Earth, planets and space*, 63(7), 815–820.

Fujita, S., Nomura, R., Moriguchi, S., Otake, Y., Koshimura, S., Leveque, R., & Terada, K. (2024, 02). Optimization of a tsunami gauge configuration for pseudo-super-resolution of wave height distribution. *Earth and Space Science*, 11. doi: 10.1029/2023EA003144

GEBCO Compilation Group. (2023). *GEBCO 2023 Grid*. (doi:10.5285/f98b053b-0cbc-6c23-e053-6c86abc0af7b)

Imamura, F., Boret, S., Suppasri, A., & Muhamari, A. (2019, 05). Recent occurrences of serious tsunami damage and the future challenges of tsunami disaster risk reduction. *Progress in Disaster Science*, 1, 100009. doi: 10.1016/j.pdisas.2019.100009

Inazu, D., & Saito, T. (2013). Simulation of distant tsunami propagation with a radial loading deformation effect. *Earth, Planets and Space*, 65, 835–842.

Kingma, D. P., & Ba, J. (2014). Adam: A method for stochastic optimization. *arXiv preprint arXiv:1412.6980*.

Lee, E., Jung, T., & Shin, S. (2020, 09). Numerical and probabilistic study on the optimal region for tsunami detection instrument deployment in the eastern sea of korea. *Applied Sciences*, 10, 6071. doi: 10.3390/app10176071

LeVeque, R. J., George, D. L., & Berger, M. J. (2011). Tsunami modelling with adaptively refined finite volume methods. *Acta Numerica*, 20, 211–289.

Lilly, J. R., Capodaglio, G., Petersen, M. R., Brus, S. R., Engwirda, D., & Higdon, R. L. (2023). Storm surge modeling as an application of local time-stepping in MPAS-Ocean. *Journal of Advances in Modeling Earth Systems*, 15(1), e2022MS003327.

Lilly, J. R., Engwirda, D., Capodaglio, G., Higdon, R. L., & Petersen, M. R. (2023). CFL Optimized Forward–Backward Runge–Kutta Schemes for the Shallow-Water Equations. *Monthly Weather Review*, 151(12), 3191–3208.

Liu, C., Rim, D., Baraldi, R., & Leveque, R. (2021, 12). Comparison of machine learning approaches for tsunami forecasting from sparse observations. *Pure and Applied Geophysics*, 178. doi: 10.1007/s00024-021-02841-9

Maeda, T., Obara, K., Shinohara, M., Kanazawa, T., & Uehira, K. (2015, 10). Successive estimation of a tsunami wavefield without earthquake source data: A data assimilation approach toward real-time tsunami forecasting. *Geophysical Research Letters*, 42. doi: 10.1002/2015GL065588

Magdalena, I., La’lang, R., Mendoza, R. G., & Lope, J. E. C. (2021). Optimal placement of tsunami sensors with depth constraint. *PeerJ Computer Science*, 7. Retrieved from <https://api.semanticscholar.org/CorpusID:240071378>

Manohar, K., Brunton, B., Kutz, J., & Brunton, S. (2018, 05). Data-driven sparse sensor placement for reconstruction. *IEEE control systems*, 38, 63-. doi: 10.1109/MCS.2018.2810460

Marcato, A., O’Malley, D., Viswanathan, H., Guiltinan, E., & Santos, J. E. (2023). *Reconstruction of fields from sparse sensing: Differentiable sensor placement enhances generalization*.

Meza, J., Catalán, P., & Tsushima, H. (2020, 03). A multiple-parameter methodology for placement of tsunami sensor networks. *Pure and Applied Geophysics*, 177. doi: 10.1007/s00024-019-02381-3

Mulia, I., Hirobe, T., Inazu, D., Endoh, T., Niwa, Y., Gusman, A., ... Hibiya, T. (2020, 02). Advanced tsunami detection and forecasting by radar on unconventional airborne observing platforms. *Scientific Reports*, 10. doi: 10.1038/s41598-020-59239-1

Mulia, I., Ueda, N., Miyoshi, T., Gusman, A., & Satake, K. (2022, 09). Machine learning-based tsunami inundation prediction derived from offshore observations. *Nature Communications*, 13, 5489. doi: 10.1038/s41467-022-33253-5

NOAA. (2011). *National Data Buoy Center – DART*. (<http://www.ndbc.noaa.gov/dart.shtml>)

Pal, N., Barton, K. N., Petersen, M. R., Brus, S. R., Engwirda, D., Arbic, B. K., ... Wirasaet, D. (2023). Barotropic tides in MPAS-Ocean (E3SM V2): impact of ice shelf cavities. *Geoscientific Model Development*, 16(4), 1297–1314.

Popinet, S. (2012). Adaptive modelling of long-distance wave propagation and fine-scale flooding during the Tohoku tsunami. *Natural Hazards and Earth System Sciences*, 12(4), 1213–1227.

Popinet, S. (2020). A vertically-Lagrangian, non-hydrostatic, multilayer model for multiscale free-surface flows. *Journal of Computational Physics*, 418, 109609.

Rim, D., Baraldi, R., Liu, C. M., LeVeque, R. J., & Terada, K. (2022). Tsunami early warning from global navigation satellite system data using convolutional neural networks. *Geophysical Research Letters*, 49(20), e2022GL099511.

Ringler, T., Thuburn, J., Klemp, J., & Skamarock, W. (2010). A unified approach to energy conservation and potential vorticity dynamics for arbitrarily-structured C-grids. *Journal of Computational Physics*, 229(9), 3065–3090.

Santos, J. E., Fox, Z. R., Mohan, A., O’Malley, D., Viswanathan, H., & Lubbers, N. (2023). Development of the Senseiver for efficient field reconstruction from sparse observations. *Nature Machine Intelligence*, 1–9.

Takahashi, N., & Imai, K. (2022, 02). Realtime tsunami prediction system using

ocean floor network for local regions. *Applied Sciences*, 12, 1627. doi: 10.3390/app12031627

Thuburn, J., Ringler, T., Skamarock, W., & Klemp, J. (2009). Numerical representation of geostrophic modes on arbitrarily structured C-grids. *Journal of Computational Physics*, 228(22), 8321 - 8335.

Titov, V. V., & Gonzalez, F. I. (1997). Implementation and testing of the method of splitting tsunami (MOST) model.

Vaswani, A., Shazeer, N. M., Parmar, N., Uszkoreit, J., Jones, L., Gomez, A. N., ... Polosukhin, I. (2017). Attention is all you need. In *Neural information processing systems*. Retrieved from <https://api.semanticscholar.org/CorpusID:13756489>

Wang, Y. (2022, 10). Green's function-based tsunami data assimilation (gftda). In (p. 19-43). doi: 10.1007/978-981-19-7339-0\_2

Wang, Y., Imai, K., Miyashita, T., Ariyoshi, K., Takahashi, N., & Satake, K. (2023, 10). Coastal tsunami prediction in tohoku region, japan, based on s-net observations using artificial neural network. *Earth Planets and Space*, 75, 154. doi: 10.1186/s40623-023-01912-6

Wang, Y., Imai, K., Mulia, I. E., Ariyoshi, K., Takahashi, N., Sasaki, K., ... Sato, Y. (2023). Data Assimilation Using High-Frequency Radar for Tsunami Early Warning: A Case Study of the 2022 Tonga Volcanic Tsunami. *Journal of Geophysical Research: Solid Earth*, 128(2), e2022JB025153.

Wang, Y., Maeda, T., Satake, K., Heidarzadeh, M., Su, H.-Y., Sheehan, A., & Gusman, A. (2019, 02). Tsunami data assimilation without a dense observation network. *Geophysical Research Letters*, 46. doi: 10.1029/2018GL080930

Xiao, H., Spica, Z., Li, J., & Zhan, Z. (2024, 01). Detection of earthquake infragravity and tsunami waves with underwater distributed acoustic sensing. *Geophysical Research Letters*, 51. doi: 10.1029/2023GL106767

Xinsheng Qin, M. R. M., Randall J. LeVeque. (2019). Accelerating an adaptive mesh refinement code for depth-averaged flows using gpus. *Journal of Advances in Modeling Earth Systems*, 11(8), 2606–2628. (<https://doi.org/10.1029/2019MS001635>)